Energy Storage Materials 67 (2024) 103320

Contents lists available at ScienceDirect

Energy Storage Materials

journal homepage: www.elsevier.com/locate/ensm

Dual-stage polyporate framework with redox mediator for high loading lithium sulfur batteries

Yifan Zhang [a,1], Wenqiang Wang [a,1], Zhichao Jia [a], Jianlong Ding [a], Lan Hua [a], Ming Sun [a], Yilin Li [a], Gengchao Wang [a,*], Chunzhong Li [b,*]

[a] Shanghai Engineering Research Center of Hierarchical Nanomaterials, Shanghai Key Laboratory of Advanced Polymeric Materials, School of Materials Science and Engineering, East China University of Science and Technology, Shanghai 200237, China

[b] Shanghai Engineering Research Center of Hierarchical Nanomaterials, School of Chemical Engineering, East China University of Science and Technology, Shanghai 200237, China

ARTICLE INFO

Keywords:
Lithium sulfur batteries
Graphene
Redox mediator
Shuttle effect
High loading

ABSTRACT

Realizing a high sulfur loading cathode is a necessary measure for assembling a high actual energy density lithium sulfur battery, which requires consideration of conductivity, reaction interface, confinement of lithium polysulfide, and redox kinetics. Herein, a pomegranate-inspired dual-stage porous graphene foam with large cavity skeletons and submicron small cavity carriers is obtained by combining the bubble-template and the flash-freezing ice-template. Furthermore, the redox mediator of poly (1-aminoanthraquinone) is electropolymerized onto it to obtain a sulfur host with high specific surface area and strong confinement capability. The nanosized sulfur deposition behavior and the rich electronic relay capability of the sulfur host are analyzed by the independent gradient model combined with in-situ Raman spectroscopy. Besides, a few of electro-depolymerization products of poly (1-aminoanthraquinone) are confirmed to be able to migrate to the anode surface to stabilize lithium deposition. With these merits, the assembled lithium sulfur batteries exhibit a discharge capacity of 1214 mAh g^{-1} and a high capacity retention rate of 75.1 % after 800 cycles at a sulfur loading of 10.0 mg cm^{-2}, and provide an excellent areal capacity of 17.5 mAh cm^{-2} (867 mAh g^{-1}) even at an ultra-high sulfur loading of 20.1 mg cm^{-2}.

1. Introduction

Electric vehicles and consumer electronics require high specific energy and long endurance batteries [1,2]. The lithium sulfur battery (LSB) system, which is matched by elemental sulfur and metallic lithium and has a theoretical energy density of up to 2600 Wh kg^{-1}, is considered a high specific energy battery system with great development prospects [3–5]. In most works of designing LSBs, the sulfur loading is always low due to the slow kinetic process and shuttle effect of sulfur [6–8]. While lithium and electrolyte are significantly excessive to meet the consumption of irreversible SEI films, which leads to low actual energy density and resource waste [9–11]. Therefore, it is necessary to design LSBs with high sulfur loading to achieve a reasonable capacity ratio of cathodes and anodes and improve the actual energy density.

However, under high sulfur loadings, the insulation of sulfur and its discharge products leads to a unacceptable decrease in the cathode electron transfer performance, and the sharp increase in active substances also leads to a serious shortage of interfaces that can be used for redox reactions [12,13]. In addition, high concentrations of soluble polysulfides (Li_2S_n) significantly increase the viscosity and resistance of electrolytes [14,15]. These seriously hinder the participation of cathode active substances in the redox process, and bring about extremely poor discharge capacity and rate performance [16]. Meanwhile, high concentrations of soluble Li_2S_n also lead to a more significant shuttle effect, which further reacts with lithium to form irreversible mossy-like deposition products with ion insulation, greatly consuming the available lithium capacity [17]. Therefore, many works use a negative/positive electrode capacity (N/P) ratio of tens of times to ensure sufficient lithium accessibility [18]. However, a limited N/P ratio is a key parameter for achieving high energy density practical LSBs [19]. Therefore, designing an ideal high loading LSB requires balancing the high conductivity of the sulfur cathode, sufficient reaction interface,

* Corresponding authors.
E-mail addresses: gengchaow@ecust.edu.cn (G. Wang), czli@ecust.edu.cn (C. Li).
[1] These authors contributed equally to this work.

https://doi.org/10.1016/j.ensm.2024.103320
Received 2 December 2023; Received in revised form 6 February 2024; Accepted 2 March 2024
Available online 3 March 2024

strong soluble Li_2S_n confinement ability, excellent redox kinetics, and good lithium deposition stability mechanism. Unfortunately, there are currently few reports on strategies that can balance the aforementioned performance.

Hitherto, numerous valuable efforts such as developing sulfur host structures, modifying binders, and preparing functionalized separators have been proposed to construct high loading LSBs [20–27]. These strategies alleviate shuttle effects by introducing components with higher binding energy to coordinate Li_2S_n; Or enhance the catalytic conversion activity of polysulfides, thereby enhancing the redox kinetics [28–30]. However, the use of modified binders or functionalized separators will inevitably induce the aggregation of sulfur species towards regions with catalytic activity, thereby altering the sulfur spatial distribution uniformity and leading to the deterioration of LSB performance [31–33]. Therefore, it is necessary to design a sulfur host with dense ultrafine cavities and strong catalytic conversion activity, so that sulfur species can be uniformly loaded and transformed in-situ at the micro scale, in order to ensure long-term uniformity of sulfur spatial distribution [34–37].

Herein, we were inspired by the phenomenon that the internal fascia of pomegranate tightly bundled the small seeds to obtain the fruit with complete structure. Through the bubble-templates, we obtained the large cavity reduced graphene oxide (rGO) foam skeletons with 3D mesh support structure. Subsequently, the submicron rGO cavities prepared by the flash-freezing ice-template were filled into the large skeletons to obtain the rGO foams with a dual-stage pore structure. And the multifunctional sulfur host (rGO-LA) was obtained by electropolymerization of poly (1-aminoanthraquinone) (PAAQ) redox mediator on its lamellae. It contained the following utilities: (1) By relying on the conversion of quinone and benzene forms, PAAQ could serve as an redox mediator to provide rich electronic relay; (2) The folded PAAQ interfaces could refine the deposition particles of sulfur during the melting sublimation process; (3) The lithium bond confinement effect of the quinonyl greatly alleviated the shuttle effect; (4) A few of electro-depolymerization products AAQ migrated to the anode surface to form an interface, stabilizing lithium deposition. Consequently, this work extended an innovative avenue for the construction of self-supporting carbon materials with multi-stage pore structures for high loading sulfur cathodes and LSBs with actual high energy density.

2. Results and discussion

A small-scale charge-reachable cavity with multiple confinement capabilities is an ideal carrier for achieving efficient sulfur conversion and stable sulfur spatial distribution. However, we found that it is difficult for reduced graphene oxide (rGO) to combine the effective sulfur loading capacity of foam with its structural support capacity. That is, when the apertures of ultrafine cavities decrease, their mechanical structure is not enough to ensure the structural stability of the rGO foams. Thus, in order to obtain a sulfur carrier with high mechanical strength and strong sulfur loading capacity, we designed a dual-stage pore-structured rGO foam, which inspired by the internal structure of pomegranate.

The preparation process of the rGO-LA high sulfur loading cathode is shown in Fig. 1. Firstly, a large cavity rGO foam framework (rGOF) with excellent conductivity and 3D mesh support structure was obtained by using the surfactant-like characteristics of graphene oxide (GO) and with the help of polyvinyl alcohol through low-pressure foam nozzle molding and high-temperature calcination, which was used as the bearing framework for small size sulfur loaded cavities. Furthermore, after fully filling the GO dispersion, it was flash-frozen by liquid nitrogen. With a nucleation temperature much lower than that of conventional freezing

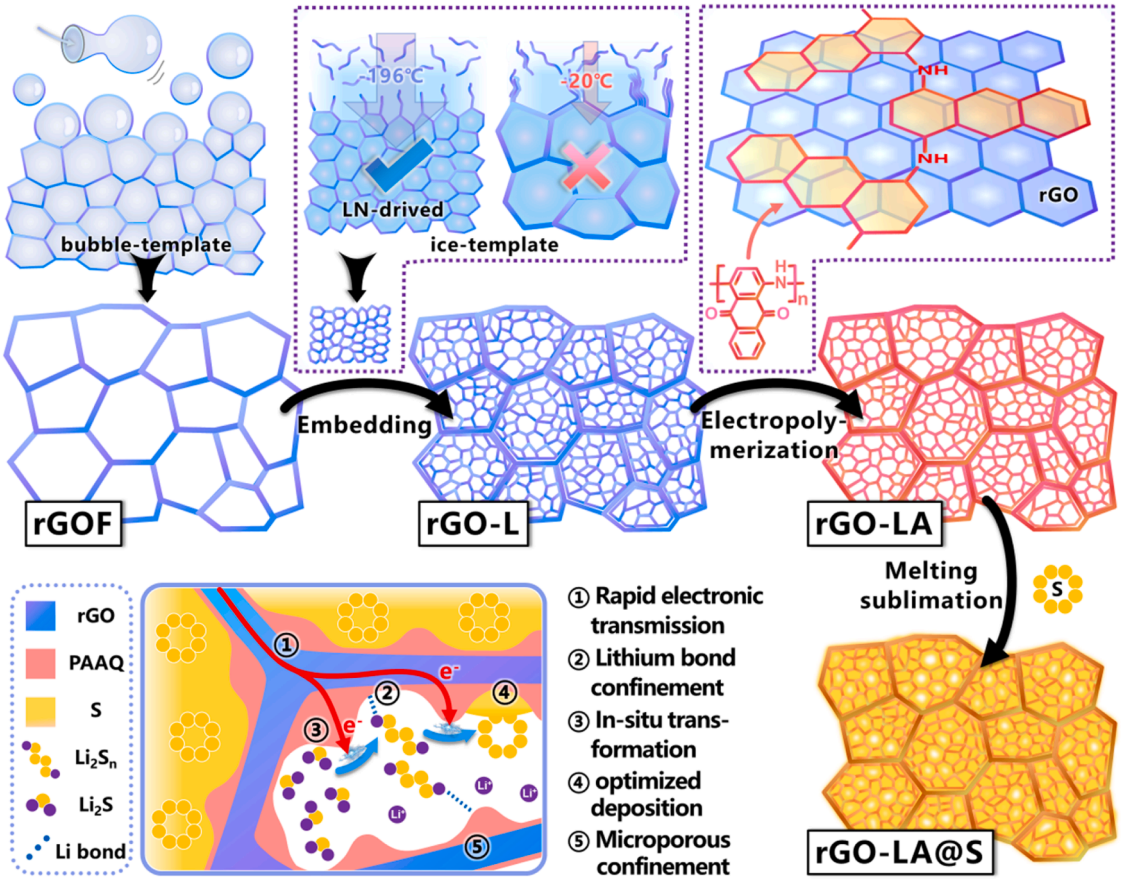

Fig. 1. Schematic diagram of preparation process and mechanism of action for the rGO-LA@S cathode.

(−196 ℃ vs. −20 ℃), the radius of ice crystals was significantly reduced, prompting the GO lamellae to overlap at the edge of submicron ice crystals. After lyophilization and calcination reduction, the rGO cavities with high specific surface area were obtained. Subsequently, PAAQ with folded morphology was modified on the rGO through electropolymerization to endow rGO with functions such as redox rich electronic relay capability, lithium-bond chemical confinement effect, and deposition behavior of nanoscale sulfur, namely a dual-stage pore-structured rGO@PAAQ sulfur host (rGO-LA) inspired by pomegranate.

Research findings that the appearances of rGOF before and after calcination are shown in Fig. S1A and Fig. S1B, respectively. The rGOF exhibits a similar pore structure to GOF, with only slight shrinkage in size. Through computer vision analysis, the pore sizes of rGOF are mostly below 0.4 mm (Fig. S1C). The compression stress-strain curve exhibites that the rGOF has excellent compression resistance and can maintain structural integrity after compression (Fig. S1D). SEM images show that the rGOF has a dense and uniform pore structure and interconnected channels (Fig. S2). These aforementioned characteristics indicate that the rGOF can effectively limit and accommodate the liquid nitrogen flash-freezing rGO particles, making it suitable as a load-bearing frame. Fig. S3 indicates that the flash-freezing foams can completely fill the cavities of rGOF, which proves that the rGOF is an excellent load-bearing frame.

The morphology of rGO foam obtained by ordinary ice-template is shown in Fig. 2A, which has a macroporous structure with a diameter of 20~50 μm. This is because during the slow freezing process, the slow growth of ice crystals intensifies the aggregation of GO lamellae caused by π-π conjugation (Fig. 2A and Fig. S4A). In contrast, the reason why

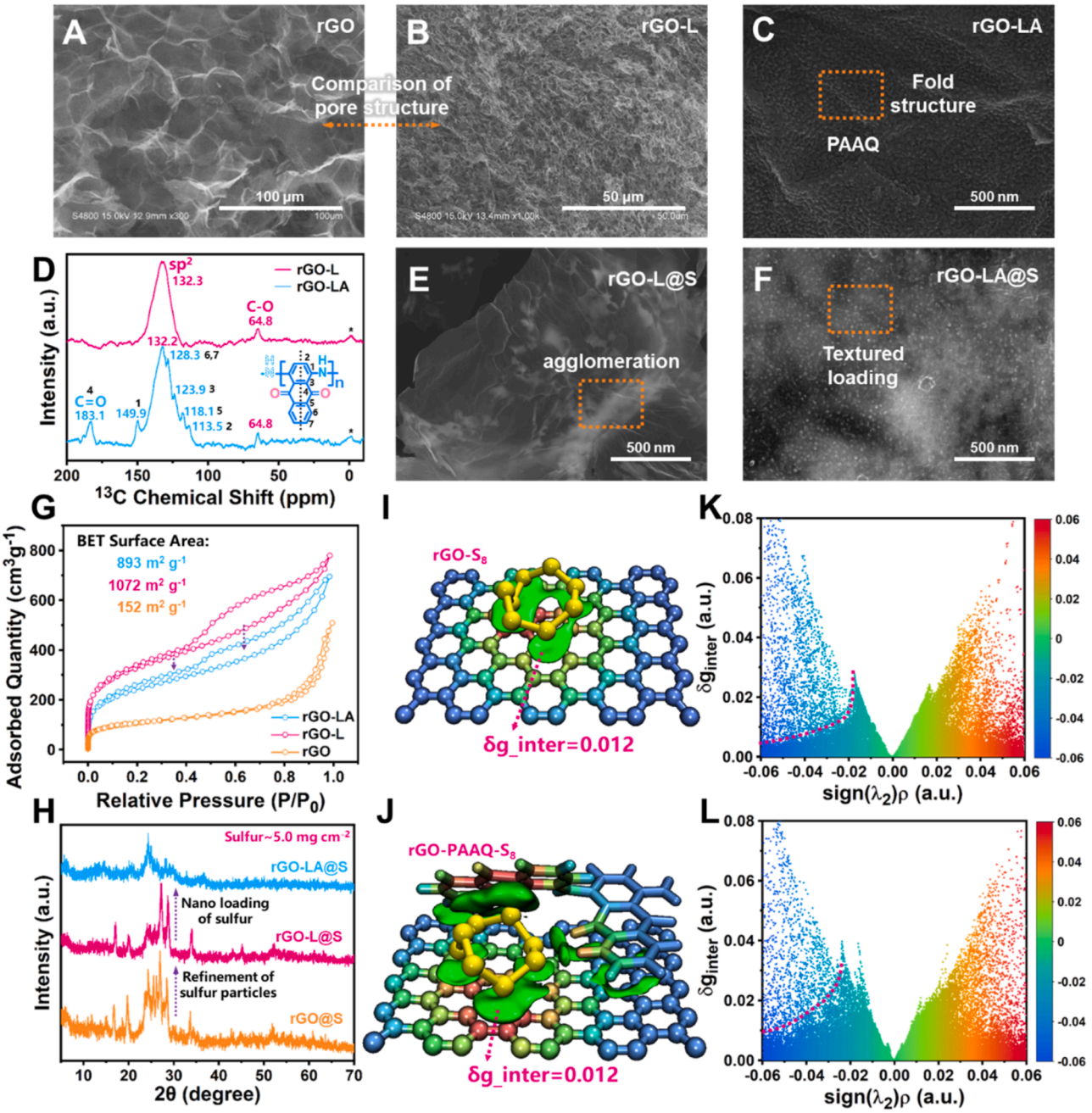

Fig. 2. FESEM images of (A) the rGO, (B) the rGO-L and (C) the lamellar details of rGO-LA. (D) Solid-state ^{13}C NMR analysis of the rGO-L and the rGO-LA. FESEM images of the (E) rGO-L@S and (F) rGO-LA@S. (G) Nitrogen adsorption-desorption isotherms, and (H) XRD patterns of rGO, rGO-L and rGO-LA. IGM isosurfaces of (I) rGO@S and (J) rGO-LA@S, and IGM point plots of regions with different electron cloud densities of (K) rGO@S and (L) rGO-LA@S.

liquid nitrogen flash-freezing densifies the stacking structure between GO lamellae can be attributed to that the GO lamellae are instantly fixed in their original position in the dispersion during the quenching process, and the thermally-driven migration process does not occur in time, resulting in the formation of a porous "micro sponge" structure (Fig. 2B and Fig. S4B, C). After electropolymerization, wrinkled PAAQ with an indentation width of dozens of nanometers can be observed adhering to the graphene lamellae. (Fig. 2C and Fig. S4D). The infrared spectrum exhibits characteristic peaks of the conjugated skeleton of the PAAQ in the wavenumber range of 1000–1800 cm^{-1} (Fig. S5). Additionally, the CP-MAS ^{13}C NMR spectrum of rGO-L reveals typical sp^2 hybridization peaks at 132.3 ppm, along with a minor residual C—O site peak at 64.8 ppm after microwave reduction (Fig. 2D) [38]. Following electro-polymerization, the spectrum of rGO-LA reveals the characteristic peaks of PAAQ at 183.1, 149.9, 128.3, 123.9, 118.1, and 113.5 ppm [39,40]. It is noteworthy that the polymerized PAAQ chain elements exhibit a symmetrical structure. The peak at 183.1 ppm originates from C = O (C-4) on the conjugated quinone ring. And the peak at 149.9, 123.9 and 118.1 ppm is attributed to non-protonated to C-1, C-3 and C-5 carbon, respectively. The peak at 128.3 ppm corresponds to C-6,7 on the conjugated benzene ring. The peak at 113.5 ppm belongs to protonated C-2 carbon. These results clearly demonstrate the successful attachment of the PAAQ to the rGO-L lamellae.

Furthermore, the differences of sulfur morphology on different foams are reflected in Fig. 2E, F and Fig. S6. Sulfur tends to form massive agglomerations on the large lamellae of ordinary rGO foams (Fig. S6A). This is the fountainhead of poor redox kinetics of ordinary rGO foam cathodes, and is also one of the primary issues that urgent to be tackled for LSBs: poor electronic conductivity caused by agglomerated sulfur blocks seriously diminishes the availability and rate performance of sulfur. As a comparison, the rGO foams of flash-freezing can partially alleviate the sulfur accumulation and promote the dispersion of small sulfur particles by reason of the enhancement of specific surface area (Fig. S6B). However, relying solely on the affinity between the graphene and the sulfur is not sufficient to propel the nanoscale deposition of sulfur (Fig. 2E and Fig. S7). Thereupon, the PAAQ was introduced with wrinkled surfaces as the attachment site for sulfur. Consequently, through the melt sublimation process, sulfur can form particles with a diameter of approximately 30 nanometers and improve the uniformity of sulfur loading (Fig. 2F and Fig. S7D). Additionally, the nucleation and growth processes of sulfur clusters confirm that the increase in nucleation sites drives the faster nucleation behavior of sulfur in the rGO-LA (Fig. S8).

One of the cruxes of the equilibrium of high sulfur loading and high redox kinetics is the high specific surface area of the rGO foams. The BET specific surface areas of the rGO, rGO-L, and rGO-LA foams are 152 $m^2 g^{-1}$, 1072 $m^2 g^{-1}$, and 893 $m^2 g^{-1}$, respectively (Fig. 2G). The desorption data based on the Barrett-Joyner-Halenda (BJH) [41] model yields pore size distributions with average pore widths of 23.1 nm, 10.0 nm, and 11.3 nm, respectively (Fig. S9). This indicates that liquid nitrogen flash-freezing significantly reduces the stacking of GO lamellae, thereby reducing pore sizes and enhancing specific surface areas. It is noteworthy that, after electro-polymerization, the hysteresis loop area of the isotherm for the rGO-LA in the high-pressure region (P/P_0=0.5~1) decreases relative to the rGO-L. This is attributed to the PAAQ blocking some of the pores. Conversely, within the low-pressure range of 0.2~0.4, the hysteresis loop area exhibits an increase (Fig. 2G). This is because the folded structure of the PAAQ provides additional micropores with diameters less than 2 nm. Furthermore, in order to provide a more detailed evaluation of the loadable specific surface area, we also conducted methylene blue adsorption experiments based on the Langmuir monolayer adsorption model in Fig. S10 (387 $m^2 g^{-1}$, 1276 $m^2 g^{-1}$, and 1148 $m^2 g^{-1}$, respectively).

The decline of the interlaminar stacking of graphene lamellae will significantly augment the specific surface area of rGO foams, and thereby supplying more sulfur loading loci and refining the particle dimensions. The refinement can also be reflected by the decrease in XRD diffraction peak intensity (Fig. 2H). And the diffraction peak of rGO-LA@S further weakens or even vanishes, manifesting that the decrease in the particle diameter of sulfur makes it difficult to accumulate into large-scale crystalline sulfur. The discrepant intensities of sulfur characteristic peaks in the Raman spectrum range of 100–250 cm^{-1} also verifies above conclusion (Fig. S11). It is noteworthy that the fluctuation peaks of rGO-LA and rGO-LA@S in the D and G bands derived from the conjugated backbones of PAAQ. The PAAQ is uniformly attached to the rGO lamellae due to the π-π conjugation between PAAQ and rGO lamellae. But the steric hindrance between PAAQ chains forces them difficult to lay flat on graphene. These generated uneven sites are beneficial for sulfur molecule loading.

To further investigate the adsorption interaction among the PAAQ, the rGO, and sulfur, an independent gradient model (IGM) analysis based on TZVP-MOLOPT-GTH basis set and DFT-D3 dispersion correction was conducted to plumb the van der Waals forces between molecular fragments [42,43]. The visualization results of Multiwfn are shown in Fig. 2I and J [44]. The green region between S_8 and rGO in Fig. 2I describes the isosurfaces with a density gradient difference between the segments of δ_g_inter = 0.012. Apparently, the forces between S_8 and rGO are relatively small and mainly interacted with several adjacent structural units on the rGO lamella. As a comparison, in the system containing PAAQ, S_8 is inclined to adhere to the gap between the PAAQ and the rGO, and the IGM isosurface area significantly dilate. This reflects that the rGO sulfur host after electropolymerization of PAAQ evidently enhances the adsorption of sulfur (Fig. 2J). The intense attraction accelerates the sulfur deposition behavior, which is conducive to the in-situ transformation of sulfur species, corresponding to the textured loading of sulfur in aforementioned SEM images. By plotting the density gradient differences between the segments in different electron cloud density regions, Fig. 2K and L were obtained. The regions with sign(λ_2)ρ greater than zero represent the repulsive force, while those of the other half represent the adsorption force. Notably, when the repulsive force of the rGO-LA system does not vary significantly, the peak height in the adsorption regions heightens prominently. And an additional peak appeares at the sign(λ_2)ρ value of −0.01, indicating that the introduction of PAAQ enhances the adsorption of sulfur by the rGO-LA foams.

Furthermore, the PAAQ can also diminish the overall bandgap width and ameliorate electron transfer performance by forming lithium bonds with the Li_2S_n. DFT calculations indicate that the addition of AAQ plainly narrows the bandgap width of Li_2S_n (Fig. 3A and Table S1). The illustration in the figure exhibits the electrostatic potential of Li_2S_n, indicating that the main force between the AAQ and the Li_2S_n is an electrostatic adsorption. In addition, the slow liquid-solid transition between the Li_2S_4 and the Li_2S is also one of the causations for the delayed rate response of LSBs. And the transition state retrieval manifests that the AAQ-Li_2S_4 system has a lower energy barrier during conversion (2.9 eV vs. 3.45 eV), indicating that the AAQ has a furtherance effect on the reduction kinetics of Li_2S_4 (Fig. 3B). Fig. 3C displays a schematic diagram of the action mechanism of PAAQ. Based on the conversion of quinone groups in its chain between quinone and benzene forms, the PAAQ is able to serve as a redox mediator. And relying on the expeditious transfer of electrons through the PAAQ, the sulfur species (Li_2S, Li_2S_n, and S_8) can overcome polarization and actualize in-situ conversion. Meanwhile, due to the formation of lithium bonds between the PAAQ and the Li_2S_n, the soluble Li_2S_n during charging and discharging is bound to the PAAQ interface, significantly confining the "shuttle effect". The reaction pathways with or without AAQ addition are demonstrated through changes in Gibbs free energy (Fig. 3D and Table S2,3). It is noteworthy that the entire reaction pathway is considered a complete reaction (even the solid-state reaction from Li_2S_2 to Li_2S) to represent the energy changes in all reaction stages. And the energy of Li_2S_8-stage is used as a benchmark for comparison. It can be found that the addition of AAQ results in the formation of energy intermediate states between different Li_2S_n conversion states in the

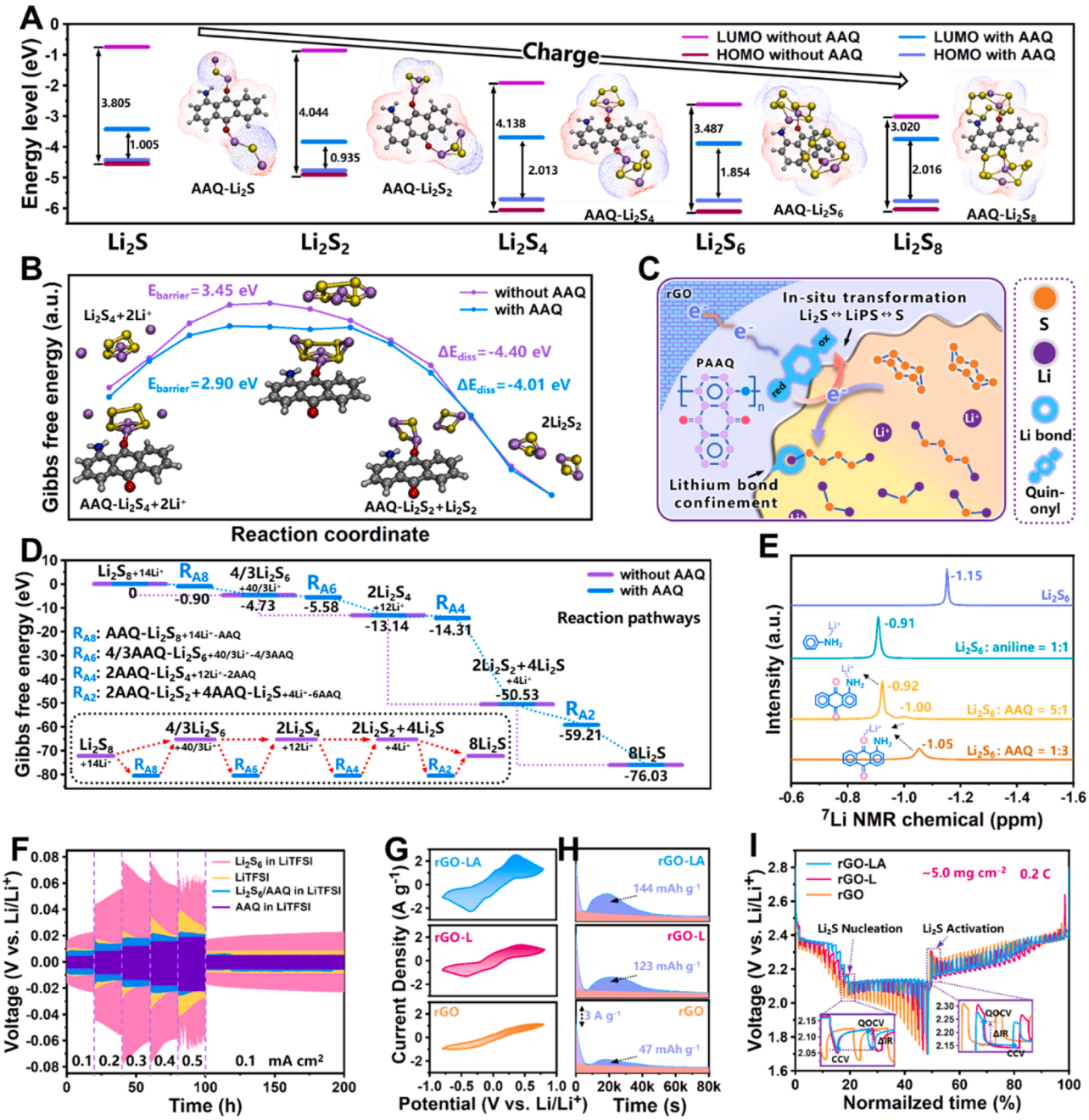

Fig. 3. (A) HOMO-LUMO energy level, and (B) transition state retrieval of the Li_2S_n with AAQ and without AAQ. (C) Schematic diagram of the action mechanism of the PAAQ. (D) Reaction pathways of the Li_2S_n with AAQ and without AAQ. (E) ^{7}Li NMR spectra of the Li_2S_6, Li_2S_6@aniline, Li_2S_6@AAQ (5:1) and Li_2S_6@AAQ (1:3). (F) Lithium deposition/stripping curves, (G) CV curves of the Li_2S_6 symmetrical batteries, (H) liquid/solid nucleation process of Li_2S, and (I) GITT curves of the rGO, rGO-L and rGO-LA batteries.

system, significantly improving the sulfur redox kinetics and rate response.

In order to verify the results of the DFT calculations, the ^{7}Li NMR analysis was adopted. The addition of AAQ results in an increase in chemical shift, attributed to the inductive effect of the quinone or amino group (Fig. 3E). Interestingly, varying the ratio of Li_2S_6 to AAQ leads to distinct NMR response characteristic peaks. When the AAQ is in excess (Li_2S_6:AAQ=1:3), all Li_2S_6 interacts with the carbonyl oxygen in AAQ through ion-dipole interactions, resulting in a chemical shift at −1.05 ppm. Conversely, when the AAQ is deficient (Li_2S_6:AAQ=5:1), the carbonyl oxygen is completely occupied, providing an opportunity for the amino group to participate in the ion-dipole interactions. This results in chemical shifts at approximately −0.92 (resembling aniline) and −1.00 (representing interactions with the carbonyl oxygen). This demonstrates the pronounced ion-dipole interaction between the AAQ and Li_2S_n.

It is noteworthy that the AAQ and the Li_2S_6 show a different blue color when mixed (Fig. S12). This is because the quinone conjugated structure in AAQ is a chromophore, and its absorption of blue light makes it red, corresponding to an electron transition of n→π*. According to the Witt chromophore theory, the unsaturated conjugated chain of AAQ acts as a chromophore when mixed with the Li_2S_6, and the S_6^{2-} containing multiple lone pair electrons acts as an auxochrome [45,46]. Therefore, the absorption peak of AAQ/Li_2S_6 shifts towards the long wavelength direction of 500 nm. And the AAQ/Li_2S_6 mixture presents its complementary color of violet, which can be confirmed in the UV–Vis

spectra (Fig. S13).

To verify the lithium bond confinement effect of AAQ on Li_2S_n, the lithium deposition/stripping tests were conducted by using LiTFSI, 0.5 M Li_2S_6 in LiTFSI, 0.1 M AAQ in LiTFSI, and 0.1 M AAQ and 0.5 M Li_2S_6 in LiTFSI as electrolytes (Fig. 3F). The polarization potential of the 0.5 M Li_2S_6 in LiTFSI electrolyte is evidently higher than that of LiTFSI due to the increase in viscosity and resistance, as well as the unstable SEI formed by Li_2S_6 on the surface of the lithium anode. However, the symmetrical battery with 0.1 M AAQ in LiTFSI performs a smaller polarization potential and prominently superior stability than the two comparison samples, LiTFSI and 0.5 M Li_2S_6 in LiTFSI. This proves that the AAQ forms a protective layer on the surface of the lithium anode, improving the stability of lithium deposition/stipping. And this is consistent with the results of DFT, as the AAQ can partially generate ion-dipole interactions with Li_2S_n, greatly confining the shuttle effect of Li_2S_n and lessening the viscosity of the electrolyte. Ulteriorly, the rGO-L electrodes exhibit a larger area in the cyclic voltammetry (CV) curve of Li_2S_6 symmetric batteries, attributing to that the incremental specific surface area allows more Li_2S_6 to participate in the redox process. The addition of PAAQ as a redox mediator further enhances the electron mediation ability between the Li_2S_6 and the rGO lamellae (Fig. 3G).

Furthermore, we explored the role of quinone groups in the transformation of sulfur species. As depicted in Fig. S14A, the oxidation potential of the benzene-to-quinone transformation in the Li//C@AAQ and Li//C@PAAQ cells, located between 2.2 V and 2.5 V, is close to that of sulfur species at 2.35 V. Similarly, the reduction potential, ranging from 2.2 V to 1.7 V, is close to that of sulfur species at 2.1 V. Therefore, the crucial factor enabling the AAQ and PAAQ to serve as redox mediators is their appropriate conversion potentials. In contrast, the Li//C@PANI cell does not exhibit significant redox peaks. Correspondingly, the C@PAAQ@Li_2S_6 symmetrical cell shows improved peak responses and redox kinetics (Fig. S14B). Hence, it can be inferred that the quinone moiety is the key functional group enabling the PAAQ to function as a redox mediator. Additionally, the stability of PAAQ in the cycles is also crucial. As depicted in Fig. S15, even after 100 cycles, the closed area and shape of the CV curves of the Li//C@PAAQ cell and the C@PAAQ@Li_2S_6 symmetrical cell exhibit no significant changes. These demonstrate that the PAAQ maintains long-term structural and functional stability in the electrochemical environment.

Therefore, during the liquid-solid nucleation process of Li_2S, the rGO-LA exhibits the maximum Li_2S deposition capacity of 144 mAh g^{-1} and a higher deposition current density (Fig. 3H). At a current density of 0.2 C, the galvanostatic intermittent titration technique (GITT) was used to investigate the charge transfer capability of different rGO cathodes during the charging/discharging process (Fig. 3I). It is evident that the rGO-LA cells show the lower ΔIR (92 mV) during the solid-liquid conversion reaction than those of the rGO-L (123 mV) and the rGO (127 mV). This indicates that the rGO-LA cells have the minimum

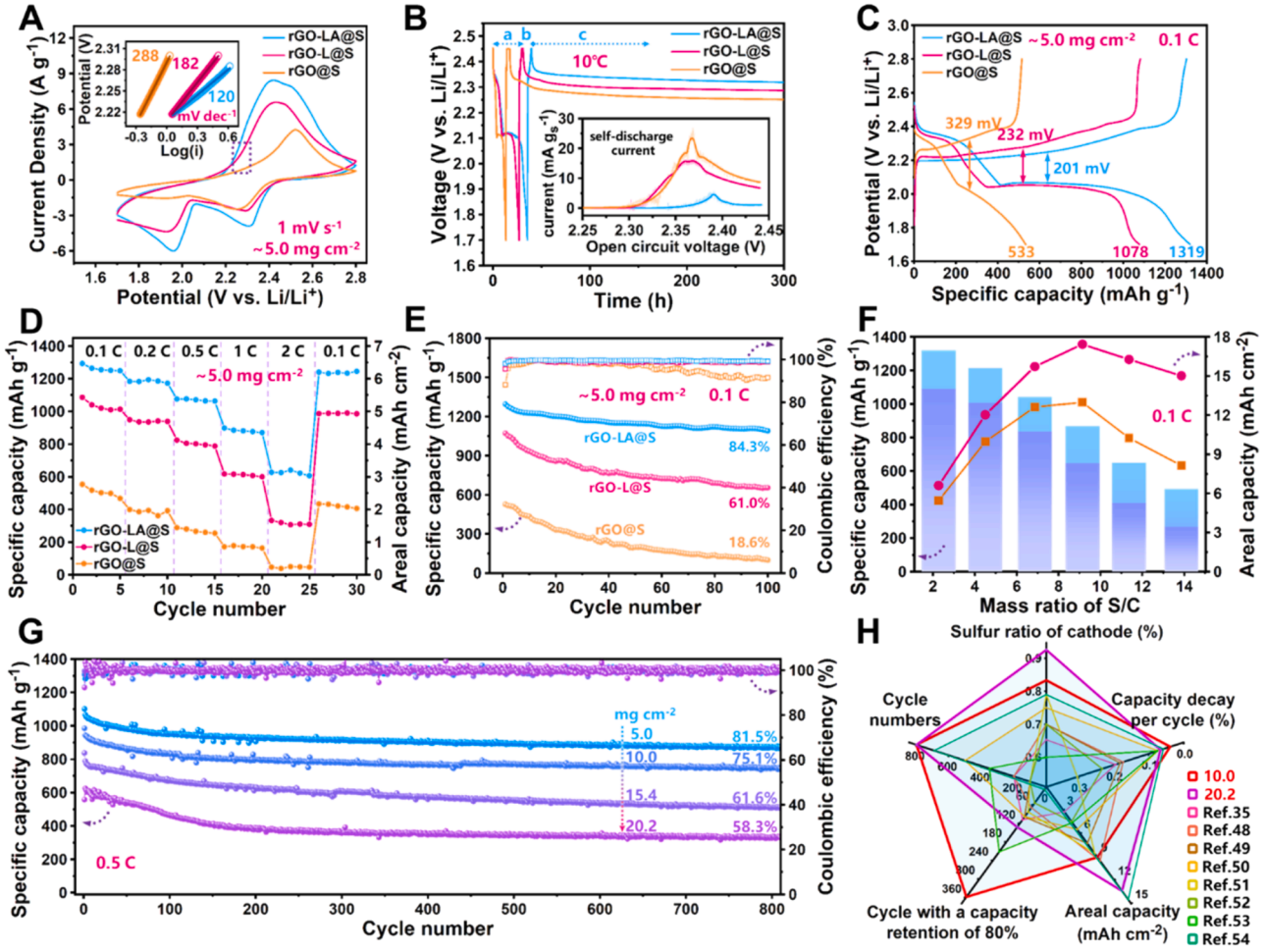

Fig. 4. (A) CV curves at a sweep rate of 1 mV s^{-1} (inset: corresponding Tafel plots), (B) the voltage variation (a: constant current discharge at C/40, b: constant current and voltage charging for 4 h, c: open circuit voltage) and the continuous shuttle current, (C) charge/discharge curves, (D) rate performance from 0.1C to 2C, and (E) cycling performance at 0.1 C of rGO@S//Li, rGO-L@S//Li and rGO-LA@S//Li cells. (F) Specific capacity and areal capacity under different S/C ratios, and (G) long-cycling performance of rGO-LA@S//Li cells with various sulfur loading capacities. (H) Comparison of comprehensive performance between this work and others.

polarization. On the one hand, this is because the finer pores obtained by liquid nitrogen flash-freezing allow the redox reaction of the system to occur in more "units". On the other hand, the PAAQ, as a redox mediator, can promptly transfer electrons to the corresponding ions or atoms, alleviating the concentration polarization.

The charge transfer resistance R_{ct} obtained by fitting the Nyquist curve shows the improved charge transfer performance of the sulfur layers attached to the rGO lamellae (Fig. S16). And the rGO-L disperses the distribution of sulfur particles and reduces the thickness of the sulfur layer by relying on fine pores and larger specific surface area, resulting in a smaller R_{ct} than rGO (32.7 Ω vs. 56.4 Ω). Compared to rGO-L, the R_{ct} of rGO-LA slightly increases. To evaluate the pore structures of the rGO foams and the influence of redox mediator PAAQ on the sulfur conversion kinetics, the CV curves at different scan rates of 0.1–1 mV s^{-1} are obtained (Fig. 4A and Fig. S17). Compared to the rGO and the rGO-L, the peak current densities of the CV curves of rGO-LA are superior, indicating that more active substances are involved in the redox process. Additionally, the splitting of the oxidation peaks of rGO-LA proves that the PAAQ can promptly convert all the homogenous Li_2S_n in the system before entering the next reaction stage. And the lower oxidation potential and higher reduction potential of rGO-LA demonstrate that the polarization of rGO-LA is relatively small. To quantify the reactivity of the reduction process at 1 mV s^{-1}, the Tafel curves are prepared in the range of 2.20 to 2.32 V. The slope of the curve of rGO-LA is 120 mV dec^{-1}, which is lower than that of rGO-L (182 mV dec^{-1}) and rGO (288 mV dec^{-1}), indicating a faster redox kinetics.

The shuttle effect of the soluble Li_2S_n in electrolytes is one of the principal causes for the irreversible deposition of active substances on lithium anodes, eventuating in abysmal capacity retention and cycle life. We conducted continuous shuttle current tests following the methodology reported by Jossen [47]. Throughout the entire open-circuit voltage testing phase (phase c), the rGO-LA battery maintains the minimal voltage drop (Fig. 4B). Correspondingly, within the voltage range of 2.3 V to 2.44 V, the rGO-LA battery exhibits the lowest continuous self-discharge current (the illustration). These findings collectively indicate that the physical confinement provided by the porous foam, coupled with the ion-dipole interaction confinement facilitated by the PAAQ.

The specific capacities obtained from the charge/discharge tests of rGO-LA, rGO-L, and rGO at 0.1 C are 1319 mAh g^{-1}, 1078 mAh g^{-1}, and 533 mAh g^{-1}, respectively (Fig. 4C). In addition, compared to the rGO-L (232 mV) and the rGO (329 mV), the rGO-LA exhibits lower overpotential (201 mV). Both demonstrate that the polyporate structure and the redox media attain exceptional reversibility and superior utilization of active substances. Fig. 4D shows the rate performance of three types of devices in the current densities range of 0.1–2 C. In all cases, the rGO-LA maintains the supreme specific capacities, demonstrating its optimal sulfur species transformation capability. After 100 cycles, the rGO-LA still retains a high specific capacity of 1112 mAh g^{-1}, with a capacity retention rate of 84.3 % (capacity damping of 0.157 % per cycle, Fig. 4E). In contrast, the rGO-L and the rGO only retain specific capacities of 667 mAh g^{-1} and 97 mAh g^{-1}, respectively, with capacity retention rates of 61.0 % (capacity damping of 0.390 % per cycle) and 18.6 % (capacity damping of 0.814 % per cycle). The superior cycling stability of rGO-LA indicates that the dense submicron pores of liquid nitrogen flash-freezing and the lithium bond adsorption effect of PAAQ on Li_2S_n synergistically confine the shuttle effect of Li_2S_n, avoiding the capacity loss of Li_2S_n on the Li anodes and the damage to the SEI films.

Currently, many researchers focus on reforming the sulfur utilization efficiency of LSBs under low loading (<1 mg cm^{-2}), but overlook the pain spot of low actual energy density of LSBs. However, in an effort to achieve an appropriate capacity ratio of cathodes and anodes and consider the extremely low cost of sulfur, we should pursue the maximum areal capacity of sulfur cathodes and the maximum actual energy density of LSBs. Accordingly, we evaluate the high loading performance of rGO-LA foams in detail. Apparently, as the sulfur loading increases from 5 mg cm^{-2} to 30.5 mg cm^{-2}, the mass specific capacities of the devices at 0.1C gradually decrease, reaching 1319 mAh g^{-1}, 1214 mAh g^{-1}, 1041 mAh g^{-1}, 867 mAh g^{-1}, 651 mAh g^{-1}, and 492 mAh g^{-1}, respectively (Fig. 4F and Fig. S18A). This is the case that as the thicknesses of the sulfur layers increase, the conductivities of the cathodes subsequently decrease (Fig. S18B). However, we find that with the increase of sulfur loading, the areal specific capacities reach a peak of 17.5 mAh cm^{-2} at 20.1 mg cm^{-2} (6.6 mAh cm^{-2}, 12.0 mAh cm^{-2}, 15.7 mAh cm^{-2}, 17.5 mAh cm^{-2}, 16.3 mAh cm^{-2}, and 15.0 mAh cm^{-2}, respectively, Fig. 4F). The long-cycling performance at 0.5 C exhibits that the devices with a surface loading of 5.0 mg cm^{-2} actualize an ultra-high capacity retention rate of 81.5 % even after 800 cycles, and it can also achieve a low capacity damping of 0.03 % during 800 cycles even at a high sulfur loading of 10.0 mg cm^{-2} (Fig. 4G). These indicate that the dense and fine pore structure and the PAAQ multifunctional interface layer can significantly limit the shuttle of Li_2S_n and maintain the structural stability of the cathodes for a long time. Therefore, when the loading reaches a maximum of 20.2 mg cm^{-2}, the devices still reap a capacity retention rate of 58.3 % after 800 cycles. In order to comprehensively compare our devices, we select five performance factors: cathode sulfur content, capacity damping per cycle, maximum number of cycles, number of cycles at a capacity retention rate of 80 %, and areal specific capacity to compare the work with others [35,48-54]. It is evident that our work exhibits the best overall performance or even the best single performance (Fig. 4H). Additionally, this work also addresses the aspects of large-scale production (Fig. S19). Besides, the cost of these foams presents a significant advantage for potential practical applications (Table S4).

Raman spectra hold a sensitive peak response to the sulfur conversion products during the charging/discharging process of LSBs. Thereby, we delved into the mechanism of PAAQ interface layer through in-situ Raman spectra at 0.5 C. Among them, Fig. 5A-C are a schematic diagram and spectra of the Raman response on the sulfur cathodes, while Fig. 5D-E are for the lithium anodes. Compared to the rGO-L, the Raman peaks of sulfur species corresponding to different stages of discharge in the rGO-LA devices exhibit higher intensities, such as the characteristic peaks of Li_2S_6 (396 cm^{-1} and 519 cm^{-1}), Li_2S_4 (198 cm^{-1}, 245 cm^{-1} and 412 cm^{-1}), Li_2S_2 (453 cm^{-1}), and Li_2S (366 cm^{-1}) [55]. Moreover, it is evident that the Raman peaks of the rGO-LA device hold a very small "tail", indicating that the redox mediator PAAQ can significantly enhance the conversion kinetics of sulfur. Relying on this, it is sufficient to reduce all sulfur species before entering the next reaction stage. In contrast, the soluble Li_2S_n in the spectra of rGO-L shows long trailing peaks, indicating that its redox kinetics is not sufficient to drive all sulfur species. This has been well corroborated in the ^{7}Li NMR spectra of sulfur species extracted through impregnation in the cathodes at different voltages (2.35 V, 2.25 V, and 2.10 V) (Fig. S20). With the decrease in potential, the increased electronegativity of terminal sulfur atoms in shorter-chain polysulfide anions enhances their deshielding effect on Li^+, leading to an increase in chemical shift [56] the NMR signal peaks exhibit similar chemical shifts (−1.18 ppm) and peak widths at 2.35 V. As the reaction progresses, they gradually reveal distinctions (−1.02 ppm vs. −1.05 ppm) at 2.1 V. Simultaneously, the signal peak width of the rGO-L cathode significantly increases while that of the rGO-LA maintains a narrower width. This unequivocally validates the enhanced redox kinetics of the rGO-LA in the in-situ Raman spectra, consequently reducing the residual unreacted Li_2S_6.

For the anodes, we expect to minimize the Li_2S_n shuttle phenomenon as much as possible. Obviously, due to the strong lithium bond confinement, there are almost no characteristic peaks of the Li_2S_n in the spectra of rGO-LA (Fig. 5E). The spectra of rGO-L expose obvious characteristic peaks of Li_2S_4 and Li_2S_6 (Fig. 5F). These shuttle soluble Li_2S_n will form solid phase Li_2S on the surface of the lithium anodes, violently affecting the electric field equilibrium of the lithium anodes and affecting the migration of lithium ions.

Through XPS analysis of the lithium anode surface after cycling, the

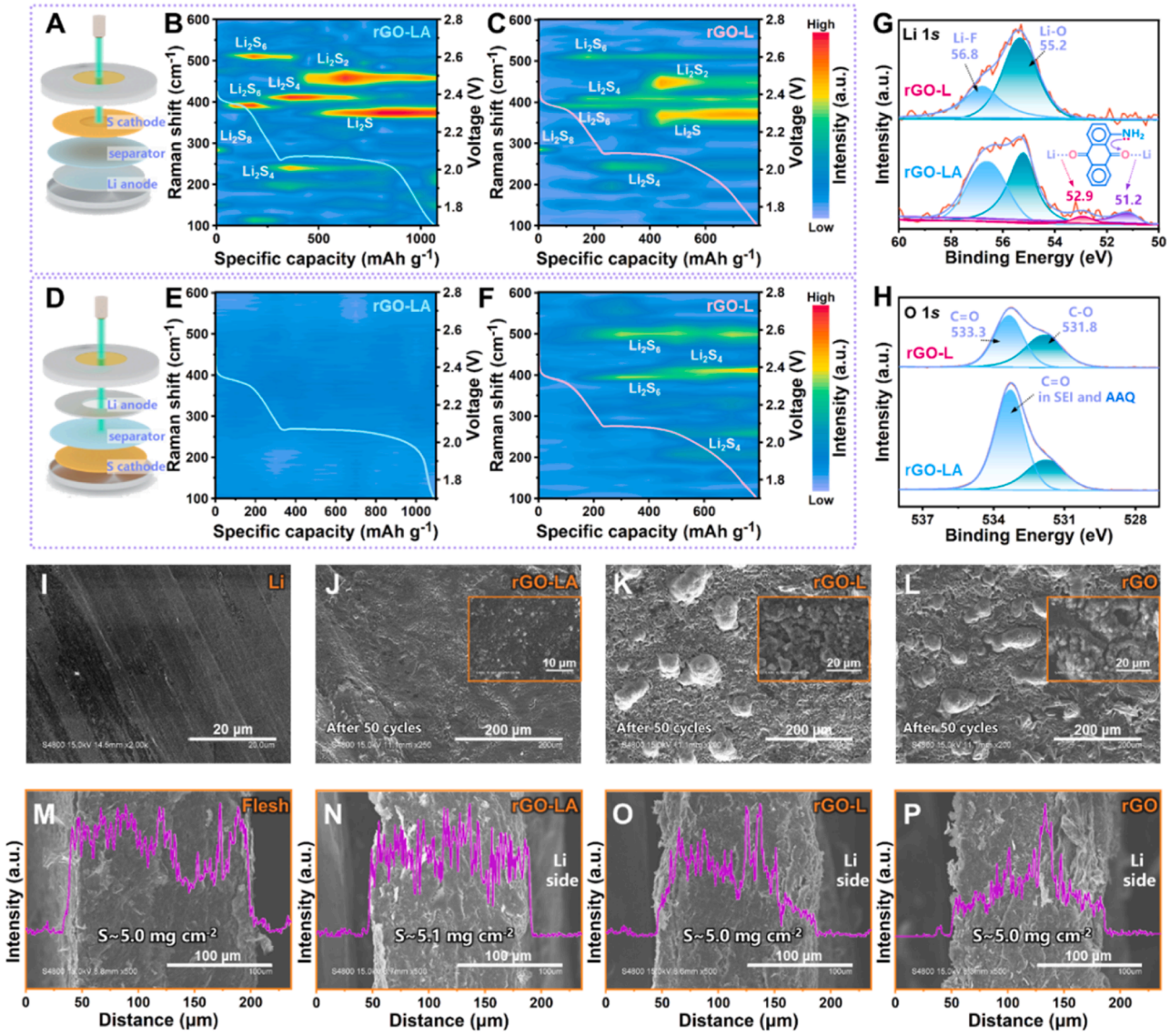

Fig. 5. (A) Schematic diagram, and in-situ Raman response on the cathode of (B) rGO-LA@S//Li and (C) rGO-L@S//Li cells. (D) Schematic diagram, and in-situ Raman response on the anode of (E) rGO-LA@S//Li and (F) rGO-L@S//Li cells. XPS spectra of (G) Li 1 *s* and (H) O 1 *s* of the rGO-LA and rGO-L. (I) FESEM images of the fresh Li anode. FESEM images of the Li anode of (J) rGO-LA@S//Li, (K) rGO-L@S//Li and (L) rGO@S//Li cells. (M) FESEM images and sulfur distribution of the fresh S cathode. FESEM images and sulfur distribution of the S cathode of (N) rGO-LA@S//Li, (O) rGO-L@S//Li and (P) rGO@S//Li cells.

elemental bonding information of the SEI film was obtained. In the Li 1 *s* spectra, due to the consistency of LiTFSI concentration, the Li-F bond strength can be used as a benchmark (Fig. 5G). The peak of the Li-O bond in rGO-L is significantly stronger than that in rGO-LA, indicating that the lithium anode surface of the rGO-LA devices exhibits superior oxidation resistance. This is because the PAAQ in rGO-LA desorbs a small amount of AAQ during the cycling process, forming a protective layer on the surface of the lithium anodes. Therefore, a lithium bond peak of AAQ complexing with Li appears in the Li 1 *s* spectrum. And there is an electron donating amino group on one side, so the binding energies of lithium bonds on both sides are also separated. The O 1 *s* spectra also prove it, as the C—O bond peak intensities on the two types of lithium anodes are relatively consistent, while the presence of AAQ significantly enhances the C = O peak of rGO-LA anodes (Fig. 5H). These small amount of electro-depolymerization products AAQ form an interface layer on the surface of the anodes. And the layer confines the Li_2S_n that occasionally escaped from the rGO-LA, providing additional lithium deposition stability and excellent lithium accessibility for high loading cathodes.

The comparison of the surface morphology of lithium anodes before and after cycling can verify the above protection mechanism (Fig. 5I-L). The surface of the fresh lithium sheet is smooth and flat (Fig. 5I). The Li_2S_n that escaped the cathode confinement in rGO and rGO-L batteries results in uneven electric fields on the lithium surfaces. Consequently, after dozens of cycles, lithium dendrites fill the lithium surface (Fig. 5K, L). On the contrary, the lithium surface of the rGO-LA batteries is flat and almost devoid of dendrites, confirming the lithium deposition stabilization provided by AAQ (Fig. 5J). In an effort to quantitatively investigate the limitations of the microporous structure and the lithium bond adsorption of Li_2S_n by the PAAQ, we conducted the EDS line scanning of sulfur elements on the cathodes after 50 cycles (Fig. 5M-P). It can be observed that the sulfur element distribution of the rGO cathode after cycling presents a "mountain peak" shape (Fig. 5P). This is because as the cycles increase, the soluble Li_2S_n shuttles and migrates to the surface of the Li anodes, leading to a decrease in capacity and an imbalance in the Li anodes electric field. As well as the rGO-L cathodes, with its tightly interwoven graphene network structure, limit a portion of Li_2S_n, but the effect is limited (Fig. 5O). Obviously, the rGO-LA

cathodes exhibit the most uniform distribution of sulfur elements (Fig. 5N). This is attributed to that the lithium bond adsorption of the PAAQ provides molecular level confinements, making it difficult for even the Li_2S_n on the near Li side to shuttle. This fully demonstrates that the rGO-LA sulfur host with small cavity physical confinement and lithium bond chemical confinement is an ideal carrier for stabilizing sulfur spatial distribution.

3. Conclusions

Inspired by pomegranate, this work combined bubble-template and flash-freezing ice-template to prepare a rGO foam with a dual-stage pore structure with high specific surface area and high conductivity. Furthermore, the redox mediator of PAAQ was electropolymerized onto it to obtain a sulfur host (rGO-LA) with strong confinement capability and in-situ conversion effect. The larger volume isosurfaces of density gradient obtained from IGM analysis and the refined sulfur deposition phenomenon in morphology analysis indicate the strong adsorption of sulfur by the rGO-LA. The narrower bandgap, lower conversion barrier, and additional intermediate states in the reaction path in DFT calculations, combined with the characteristic peak responses of in-situ Raman spectra, demonstrate that the rGO-LA can improve the electron transfer and drive efficient in-situ conversion of sulfur species. The lower lithium deposition/stripping potential and flat lithium anode morphology demonstrate that a few of electro-depolymerization products AAQ can stabilize lithium deposition. Benefitting from the above merits, the assembled rGO-LA@S//Li batteries achieve a discharge capacity of 1214 mAh g^{-1} with a sulfur loading of 10.0 mg cm^{-2} at 0.1C, as well as a low capacity damping of 0.03 % per cycle over 800 cycles at 0.5 C. And even at an ultra-high sulfur loading of 20.1 mg cm^{-2}, it can provide a superior surface capacity of 17.5 mAh cm^{-2}. This work emphasizes the excellent effect of the rGO foam composite the redox mediators with a dual-stage pore structure in enhancing the electrochemical activity of sulfur cathode. And this concept provides a new opportunity for the structural design of ultrahigh sulfur content cathode.

4. Experimental section

4.1. Preparation of the GO dispersion

The method of preparation of GO dispersion was shown in the supporting information.

4.2. Preparation of the rGO-L foam

Firstly, 5 g of GO dispersion (~5.5 mg ml^{-1}) was added to 1 g of polyvinyl alcohol aqueous solution (PVA, 2 %, Chenqi Chemical Technology Co., Ltd, Shanghai) and uniformly dispersed by ultrasonic. Next, the rGO macroporous bubble-template framework (rGOF) was obtained by spraying foam into the mold through a low-pressure foam nozzle, freeze-drying, and then intermittent vacuum microwave reduction for 5 s. Then the frame was filled with GO dispersion through vacuum suction. After that, it was frozen by the liquid nitrogen, and whose complete freezing time was controlled to about 25 s. Then it was reduced by intermittent vacuum microwave for 10 s to obtain the dual-stage pore-structured rGO-L foam. For comparison, the rGO foam without the rGOF was prepared by slow freezing at the temperature of about −20 ℃.

4.3. Preparation of the rGO-LA foam by electro-polymerization

An acetonitrile (CH_3CN, Macklin Co., Ltd) solution containing 2 mM 1-aminoanthraquinone (AAQ, Alfa Aesar), 0.2 M camphorsulfonic acid (Sinopharm Chemical Reagent Co.Ltd.) and 0.04 M tetraethyl ammonium tetrafluoroborate (Macklin Co., Ltd) was prepared. The rGO-L foam was immersed in the above solution for 2 h. And then the foam was used as the working electrode, Ag/Ag^+ electrode (containing CH_3CN solution with 0.01 M $AgNO_3$) was used as the reference electrode, and the platinum plate was used as the counter electrode. The electro-polymerization was conducted at 0.8 V for 150 s. Subsequently, the rGO-LA was obtained after fully washing with the deionized water and freeze-drying.

4.4. Loading of sulfur and assembly of the LSBs

The sulfur loading adopted high-temperature melting sublimation method. Firstly, a certain amount (usually 120 % of the expectant loading mass) of sulfur powder (Macklin Co., Ltd) was evenly spread on the foams. Then the sulfur was melted at 155 ℃ in Ar atmosphere and uniformly dispersed in the rGO lamellae to obtain cathode foam. Afterwards, the LSBs were assembled using the lithium sheets as the anodes, the Celgard 2400 as the separators, and 0.5 M LiTFSI and 1 vol% lithium nitrate ($LiNO_3$) dissolved in DOL/DME (1:1, V:V) solution as the electrolyte. The dosage of electrolyte was: when the sulfur loading was less than 15 mg cm^{-2}, the ratio of electrolyte/sulfur E: S was 10 μL mg_S^{-1}; When the sulfur loading exceeded 15 mg cm^{-2}, the electrolyte dosage remained at 150 μL.

4.5. Characterization, theoretical calculation and electrochemical measurements

The details of the characterization, theoretical calculation and electrochemical measurements were exhibited in the supporting information.

CRediT authorship contribution statement

Yifan Zhang: Writing – original draft, Methodology, Formal analysis, Data curation. **Wenqiang Wang:** Writing – review & editing, Methodology, Funding acquisition. **Zhichao Jia:** Software, Data curation. **Jianlong Ding:** Software, Formal analysis. **Lan Hua:** Software, Formal analysis. **Ming Sun:** Visualization. **Yilin Li:** Formal analysis. **Gengchao Wang:** Writing – review & editing, Funding acquisition. **Chunzhong Li:** Writing – review & editing.

Declaration of competing interest

The authors declare that they have no known competing financial interests or personal relationships that could have appeared to influence the work reported in this paper.

Data availability

Data will be made available on request.

Acknowledgements

We greatly appreciate the financial supports of National Natural Science Foundation of China (22109045, 21875065) and the China Postdoctoral Science Foundation Special Fund (2022T150211). The authors would like to thank Y. Kang from the Analysis and Testing Center of ECUST.

Supplementary materials

Supplementary material associated with this article can be found, in the online version, at doi:10.1016/j.ensm.2024.103320.

References

[1] X.Y. Yue, Y.X. Yao, J. Zhang, Z. Li, S.Y. Yang, X.L. Li, C. Yan, Q. Zhang, The Raw Mixed Conducting Interphase Affords Effective Prelithiation in Working Batteries, Angew. Chem. Int. Ed. 61 (2022) e202205697.

[2] X. Fang, W. Weng, J. Ren, H. Peng, A Cable-Shaped Lithium Sulfur Battery, Adv. Mater. 28 (2015) 491–496.

[3] L.P. Hou, H. Yuan, C.Z. Zhao, L. Xu, G.L. Zhu, H.X. Nan, X.B. Cheng, Q.B. Liu, C. X. He, J.Q. Huang, Q. Zhang, Improved interfacial electronic contacts powering high sulfur utilization in all-solid-state lithium-sulfur batteries, Energy Storage Mater 25 (2020) 436–442.

[4] Y.H. Liu, W. Chang, J. Qu, Y.Q. Sui, Y. Abdelkrim, H.J. Liu, X.Z. Zhai, Y.G. Guo, Z. Z. Yu, A polymer organosulfur redox mediator for high-performance lithium-sulfur batteries, Energy Storage Mater 46 (2022) 313–321.

[5] X.W. Wang, C.H. Yang, X.H. Xiong, G.L. Chen, M.Z. Huang, J.H. Wang, Y. Liu, M. L. Liu, K. Huang, A robust sulfur host with dual lithium polysulfide immobilization mechanism for long cycle life and high capacity Li-S batteries, Energy Storage Mater 16 (2019) 344–353.

[6] S. Feng, Z.H. Fu, X. Chen, B.Q. Li, H.J. Peng, N. Yao, X. Shen, L.G. Yu, Y.C. Gao, R. Zhang, Q. Zhang, An Electrocatalytic Model of the Sulfur Reduction Reaction in Lithium-Sulfur Batteries, Angew. Chem. Int. Ed. 61 (2022) e202211448.

[7] H. Sul, A. Bhargav, A. Manthiram, Lithium Trithiocarbonate as a Dual-Function Electrode Material for High-Performance Lithium–Sulfur Batteries, Adv. Energy Mater. 12 (2022) 202200680.

[8] T. Wang, D. Su, Y. Chen, K. Yan, L. Yu, L. Liu, Y. Zhong, P.H.L. Notten, C. Wang, G. Wang, Biomimetic 3D Fe/CeO_2 decorated N-doped carbon nanotubes architectures for high-performance lithium-sulfur batteries, Chem. Eng. J. 401 (2020) 126079.

[9] S. Nanda, A. Bhargav, A. Manthiram, Anode-free, Lean-Electrolyte Lithium-Sulfur Batteries Enabled by Tellurium-Stabilized Lithium Deposition, Joule 4 (2020) 1121–1135.

[10] L.P. Hou, N. Yao, J. Xie, P. Shi, S.Y. Sun, C.B. Jin, C.M. Chen, Q.B. Liu, B.Q. Li, X. Q. Zhang, Q. Zhang, Modification of Nitrate Ion Enables Stable Solid Electrolyte Interphase in Lithium Metal Batteries, Angew. Chem. Int. Ed. 61 (2022) e202201406.

[11] H. Chen, A. Pei, D. Lin, J. Xie, A. Yang, J. Xu, K. Lin, J. Wang, H. Wang, F. Shi, D. Boyle, Y. Cui, Uniform High Ionic Conducting Lithium Sulfide Protection Layer for Stable Lithium Metal Anode, Adv. Energy Mater. 9 (2019) 201900858.

[12] L. Wang, M. Zhen, Z. Hu, Status and prospects of electrocatalysts for lithium-sulfur battery under lean electrolyte and high sulfur loading conditions, Chem. Eng. J. 452 (2023) 139344.

[13] H. Qiu, T. Wang, W. Lv, Q. Liu, J. Huang, Three-dimensional carbon foam decorated with SnO_2 as multifunctional host for lithium sulfur batteries, J. Colloid Interface Sci. 630 (2023) 106–114.

[14] R. Guo, Y. Yang, X.L. Huang, C. Zhao, B. Hu, F. Huo, H.K. Liu, B. Sun, Z. Sun, S. X. Dou, Recent Advances in Multifunctional Binders for High Sulfur Loading Lithium-Sulfur Batteries, Adv. Funct. Mater. (2023) 202307108.

[15] Z. Chu, X. Gao, C. Wang, T. Wang, G. Wang, Metal–organic frameworks as separators and electrolytes for lithium–sulfur batteries, J. Mater. Chem. A 9 (2021) 7301–7316.

[16] M. Wang, Z. Bai, T. Yang, C. Nie, X. Xu, Y. Wang, J. Yang, S. Dou, N. Wang, Advances in High Sulfur Loading Cathodes for Practical Lithium-Sulfur Batteries, Adv. Energy Mater. 12 (2022) 202201585.

[17] S. Hu, T. Wang, B. Lu, D. Wu, H. Wang, X. Liu, J. Zhang, Ionic-Liquid-Assisted Synthesis of FeSe–MnSe Heterointerfaces with Abundant Se Vacancies Embedded in N,B Co-Doped Hollow Carbon Microspheres for Accelerating the Sulfur Reduction Reaction, Adv. Mater. 34 (2022) 202204147.

[18] S.R. Chen, Y. Gao, Z.X. Yu, M.L. Gordin, J.X. Song, D.H. Wang, High capacity of lithium-sulfur batteries at low electrolyte/sulfur ratio enabled by an organosulfide containing electrolyte, Nano Energy 31 (2017) 418–423.

[19] Y. Ren, A. Bhargav, W. Shin, H. Sul, A. Manthiram, Anode-Free Lithium–Sulfur Cells Enabled by Rationally Tuning Lithium Polysulfide Molecules, Angew. Chem. Int. Ed. 61 (2022) e202207907.

[20] R. Chu, T.T. Nguyen, Y. Bai, N.H. Kim, J.H. Lee, Uniformly Controlled Treble Boundary Using Enriched Adsorption Sites and Accelerated Catalyst Cathode for Robust Lithium–Sulfur Batteries, Adv. Energy Mater. 12 (2022) 202102805.

[21] B. Wang, L. Wang, B. Zhang, S. Zeng, F. Tian, J. Dou, Y. Qian, L. Xu, Niobium Diboride Nanoparticles Accelerating Polysulfide Conversion and Directing Li_2S Nucleation Enabled High Areal Capacity Lithium–Sulfur Batteries, ACS Nano 16 (2022) 4947–4960.

[22] J. Zhang, J. Hu, X. Li, L. Yang, L. Yang, J. Lin, J. Huang, G. Xu, High-performance MoS_2 quantum dots/graphene functionalized separator and its failure analysis under high sulfur loading, Chem. Eng. J. (2023) 456.

[23] J.H. Bae, S.R. Lee, H.Y. Choi, J.W. Park, B.G. Kim, D. Kim, S.Y. Yoon, Y.J. Lee, 3D interconnected structure-based lithium–sulfur batteries with high energy densities, Appl. Surf. Sci. 614 (2023) 156112.

[24] H. Chen, X. Zhang, S. Li, Y. Zheng, Free-Standing Sulfur Cathodes Enabled by a Cationic Polymer for Lean Electrolyte Lithium–Sulfur Batteries, ACS Energy Lett 8 (2022) 619–627.

[25] S. Gu, H. Jiang, X. Li, Y. Dai, W. Zheng, X. Jiang, G. He, Dispersing single-layered $Ti_3C_2T_X$ nanosheets in hierarchically-porous membrane for high-efficiency Li^+ transporting and polysulfide anchoring in Li-S batteries, Energy Storage Mater 53 (2022) 32–41.

[26] Y. Li, Y. Lu, X. Jiang, L. Lu, J. Qin, D. Yang, J.L. Chen, L. Zhang, D. Wang, A. Lei, Engineering vacancy-defect atomic Ni sites via biowaste valorisation for high-power kinetics in lithium-sulfur batteries, Energy Storage Mater 54 (2023) 553–562.

[27] B. Wang, L. Wang, B. Zhang, Z. Kong, S. Zeng, M. Zhao, Y. Qian, L. Xu, Ultrafine zirconium boride nanoparticles constructed bidirectional catalyst for ultrafast and long-lived lithium-sulfur batteries, Energy Storage Mater 45 (2022) 130–141.

[28] W. Yan, J.L. Yang, X. Xiong, L. Fu, Y. Chen, Z. Wang, Y. Zhu, J.W. Zhao, T. Wang, Y. Wu, Versatile Asymmetric Separator with Dendrite-Free Alloy Anode Enables High-Performance Li–S Batteries, Adv. Sci. 9 (2022) 202202204.

[29] Y. Wang, L. Zhu, J. Wang, Z. Zhang, J. Yu, Z. Yang, Enhanced chemisorption and catalytic conversion of polysulfides via CoFe@NC nanocubes modified separator for superior Li–S batteries, Chem. Eng. J. 433 (2022) 133792.

[30] W. Wang, K. Xi, B. Li, H. Li, S. Liu, J. Wang, H. Zhao, H. Li, A.M. Abdelkader, X. Gao, G. Li, A Sustainable Multipurpose Separator Directed Against the Shuttle Effect of Polysulfides for High-Performance Lithium–Sulfur Batteries, Adv. Energy Mater. 12 (2022) 202200160.

[31] X. Qiao, C. Wang, J. Zang, B. Guo, Y. Zheng, R. Zhang, J. Cui, X. Fang, Conductive inks composed of multicomponent carbon nanomaterials and hydrophilic polymer binders for high-energy-density lithium-sulfur batteries, Energy Storage Mater 49 (2022) 236–245.

[32] Z. Zhang, J. Mo, P. Yu, L. Feng, Y. Wang, Y. Lu, W. Yang, High-Performance Flexible Sulfur Cathodes with Robust Electrode Skeletons Built by a Hierarchical Self-Assembling Slurry, Adv. Sci. 9 (2022) 202201881.

[33] Q. Gong, L. Hou, T. Li, Y. Jiao, P. Wu, Regulating the Molecular Interactions in Polymer Binder for High-Performance Lithium–Sulfur Batteries, ACS Nano 16 (2022) 8449–8460.

[34] K. Zhang, X. Li, Y. Yang, Z. Chen, L. Ma, Y. Zhao, Y. Yuan, F. Chen, X. Wang, K. Xie, K.P. Loh, High Loading Sulfur Cathodes by Reactive-Type Polymer Tubes for High-Performance Lithium-Sulfur Batteries, Adv. Funct. Mater. 33 (2022) 202212759.

[35] C. Huang, J. Yu, C. Li, Z. Cui, C. Zhang, C. Zhang, B. Nan, J. Li, J. Arbiol, A. Cabot, Combined Defect and Heterojunction Engineering in ZnTe/$CoTe_2$@NC Sulfur Hosts Toward Robust Lithium–Sulfur Batteries, Adv. Funct. Mater. (2023) 202305624.

[36] J. Wu, J. Huang, Y. Cui, D. Miao, X. Ke, Y. Lu, D. Wu, Rough Endoplasmic Reticulum Inspired Polystyrene-Brush-Based Superhigh Sulfur Content Cathodes Enable Lithium–Sulfur Cells with High Mass and Capacity Loading, Adv. Mater. 35 (2023) 202211471.

[37] C. Wang, R. Liu, Y. Fang, W. Yang, F. Jin, M. Gu, D. Zhang, L. He, W. Liu, J. Chen, X. Lin, X. Feng, Y. Ma, Free-Standing Titanium Nitride Films as Carbon-Free Sulfur Hosts for Flexible Lithium–Sulfur Batteries, ACS Appl. Nano Mater. 5 (2022) 3531–3540.

[38] H. Ando, K. Suzuki, H. Kaji, T. Kambe, Y. Nishina, C. Nakano, K. Gotoh, Dynamic nuclear polarization – nuclear magnetic resonance for analyzing surface functional groups on carbonaceous materials, Carbon N Y 206 (2023) 84–93.

[39] Z. Zujovic, P.A. Kilmartin, J. Travas-Sejdic, The Applications of Solid-State NMR to Conducting Polymers. The Special Case on Polyaniline, Molecules 25 (2020).

[40] W.B.S. van Liemt, G.J. Boender, P. Gast, A.J. Hoff, J. Lugtenburg, H.J.M. de Groot, ^{13}C Magic Angle Spinning NMR Characterization of the Functionally Asymmetric QA Binding in Rhodobacter sphaeroides R26 Photosynthetic Reaction Centers Using Site-Specific ^{13}C-Labeled Ubiquinone-10, Biochemistry 34 (2002) 10229–10236.

[41] R. Bardestani, G.S. Patience, S. Kaliaguine, Experimental methods in chemical engineering: specific surface area and pore size distribution measurements-BET, BJH, and DFT, Can. J. Chem. Eng. 97 (2019) 2781–2791.

[42] T. Lu, Q.X. Chen, Independent gradient model based on Hirshfeld partition: a new method for visual study of interactions in chemical systems, J. Comput. Chem. 43 (2022) 539–555.

[43] C. Lefebvre, G. Rubez, H. Khartabil, J.C. Boisson, J. Contreras-Garcia, E. Henon, Accurately extracting the signature of intermolecular interactions present in the NCI plot of the reduced density gradient versus electron density, PCCP 19 (2017) 17928–17936.

[44] T. Lu, F.W. Chen, Multiwfn: a multifunctional wavefunction analyzer, J. Comput. Chem. 33 (2012) 580–592.

[45] F. Vázquez-Ortega, I. Lagunes, A. Trigos, Cosmetic dyes as potential photosensitizers of singlet oxygen generation, Dyes Pigm 176 (2020) 108248.

[46] Z.Q. Wang, C. Li, H.L. Zhang, Z. Liu, 1-Aminoanthraquinone Diazonium Salt on the Coupling Modification Dyeing of Silk Fibroin with Enhanced Color Fastness, Fibers Polym 19 (2018) 2134–2138.

[47] C. Maurer, W. Commerell, A. Hintennach, A. Jossen, Continuous Shuttle Current Measurement Method for Lithium Sulfur Cells, J. Electrochem. Soc. 167 (2020) 090534.

[48] N. Wang, X. Zhang, Z. Ju, X. Yu, Y. Wang, Y. Du, Z. Bai, S. Dou, G. Yu, Thickness-independent scalable high-performance Li-S batteries with high areal sulfur loading via electron-enriched carbon framework, Nat. Commun. 12 (2021) 4519.

[49] C. Zhang, B. Fei, D. Yang, H. Zhan, J. Wang, J. Diao, J. Li, G. Henkelman, D. Cai, J. J. Biendicho, J.R. Morante, A. Cabot, Robust Lithium–Sulfur Batteries Enabled by Highly Conductive WSe_2-Based Superlattices with Tunable Interlayer Space, Adv. Funct. Mater. 32 (2022) 202201322.

[50] L. Ren, J. Liu, Y. Zhao, Y. Wang, X. Lu, M. Zhou, G. Zhang, W. Liu, H. Xu, X. Sun, Regulating Electronic Structure of Fe–N_4 Single Atomic Catalyst via Neighboring Sulfur Doping for High Performance Lithium–Sulfur Batteries, Adv. Funct. Mater. 33 (2023) 202210509.

[51] V.P. Nguyen, J.S. Park, H.C. Shim, J.M. Yuk, J.H. Kim, D. Kim, S.M. Lee, Accelerated Sulfur Evolution Reactions by TiS_2/TiO_2@MXene Host for High-Volumetric-Energy-Density Lithium–Sulfur Batteries, Adv. Funct. Mater. 33 (2023) 202303503.

[52] Z.Y. Wang, H.M. Wang, S. Liu, G.R. Li, X.P. Gao, To Promote the Catalytic Conversion of Polysulfides Using Ni–B Alloy Nanoparticles on Carbon Nanotube

Microspheres under High Sulfur Loading and a Lean Electrolyte, ACS Appl. Mater. Interfaces 13 (2021) 20222–20232.
[53] M. Shaibani, M.S. Mirshekarloo, R. Singh, C.D. Easton, M.C.D. Cooray, N. Eshraghi, T. Abendroth, S. Dorfler, H. Althues, S. Kaskel, A.F. Hollenkamp, M.R. Hill, M. Majumder, Expansion-tolerant architectures for stable cycling of ultrahigh-loading sulfur cathodes in lithium-sulfur batteries, Sci. Adv. 6 (2020) eaay2757.
[54] Z. Chen, M. Lu, Y. Qian, Y. Yang, J. Liu, Z. Lin, D. Yang, J. Lu, X. Qiu, Ultra-Low Dosage Lignin Binder for Practical Lithium–Sulfur Batteries, Adv. Energy Mater. 13 (2023) 202300092.
[55] P. Chen, T. Wang, D. He, T. Shi, M. Chen, K. Fang, H. Lin, J. Wang, C. Wang, H. Pang, Delocalized Isoelectronic Heterostructured $FeCoO_xS_y$ Catalysts with Tunable Electron Density for Accelerated Sulfur Redox Kinetics in Li-S batteries, Angew. Chem. Int. Ed. 62 (2023) e202311693.
[56] A. Dorai, J. Kawamura, T. Omata, Visualization of polysulfide dissolution in lithium-sulfur batteries using in-situ NMR microimaging, Electrochem. Commun. 141 (2022) 107360.